Bridging classical and quantum approaches for quantitative sensing of turbid media with polarization-entangled photons

Vira R. Besaga[1*†], Ivan V. Lopushenko[2*†], Oleksii Sieryi[2], Alexander Bykov[2], Frank Setzpfandt[1,3], Igor Meglinski[4]

[1]Institute of Applied Physics & Abbe Center of Photonics, Friedrich Schiller University Jena, Jena 07745, Germany.

[2]Opto-Electronics and Measurement Techniques, University of Oulu, Oulu FI-90014, Finland.

[3]Fraunhofer Institute for Applied Optics and Precision Engineering IOF, Jena 07745, Germany.

[4]College of Engineering and Physical Sciences, Aston University, Birmingham B4 7ET, UK.

[*]Corresponding authors. Email: vira.besaga@uni-jena.de and ivan.lopushenko@oulu.fi

[†]These authors contributed equally to this work.

Keywords: *quantum sensing, polarization-entangled photons, coherency matrix, density matrix, scattering, Monte Carlo*

Polarimetry with quantum light promises improved measurements for various scenarios. However, fundamental understanding of quantum photonic state transport in complex, real media and tools to interpret the state after interaction with the sample are still lacking. Here, we theoretically and experimentally explore the evolution of polarization-entangled states in a turbid medium on example of tissue phantoms. By elaborating mathematical relationship between Wolf's coherency matrix and density matrix, we introduce a versatile framework describing the transfer of entangled photons in turbid environments with polarization tracking and resulting quantum state representation with the density operator. Experimentally, we reveal a robust trend in the state evolution depending on the reduced scattering coefficient of the medium. Our theoretical predictions correlate with experimental findings, while the model extends the study by photonic states with different degrees of entanglement. The presented results pave the way for quantitative quantum photonic sensing enabling applications ranging from biomedical diagnostics to remote sensing.

Read at the publisher: https://doi.org/10.1002/lpor.202501172

Introduction

Media as diverse as atmospheric aerosols, particulate matter, and biological tissues can all be described as scattering, or more generally, turbid. Optical characterization of such environments proved crucial for free-space optical communication (*1, 2*), environmental monitoring (*3, 4*), and biomedical sensing (*5, 6*). Often challenged by the high optical losses, sensing of such media by examining the polarization response known as optical polarimetry (*7*) can be particularly advantageous. This technique provides insight into the chirality, anisotropy, and morphology of the sample and is well-acknowledged for technical inspection, biomedical diagnostics, and remote sensing (*8–11*).

The versatility of polarization-based sensing fundamentally relies on a deep understanding of light propagation in complex scattering media, where classical optical polarimetry has provided crucial insights through decades of research. It has been shown that different optical parameters describing the turbid medium – scattering anisotropy factor, scattering coefficient, photon transport mean free path, and others (*12–14*) – can be related to Stokes vector and degree of polarization (DoP) measurements (*6, 15, 16*). The latter can then be used to reliably distinguish different scattering media under study, e.g. healthy tissue domains from the domains affected by disease-related morphological changes (*9*). It has been also established that certain polarization states preferentially survive multiple scattering events, a phenomenon known as polarization memory (*12*), while others rapidly depolarize. For biological tissues exhibiting strong forward scattering (*17*), this effect has enabled polarization-gating techniques that enhance imaging contrast and depth penetration (*18*). It has been revealed, that the degree of polarization memory depends critically on the scattering properties of the sample under study and choice of the polarization state for probing (*12–14*). For example, circular polarization retains its memory longer in large-scatterer media because forward scattering weakly perturbs photon helicity, while linear polarization rapidly decoheres due to phase scrambling between orthogonal components (*19, 20*). At the same time, other structured degrees of freedom of light beyond polarization exhibit analogous memory effects, e.g. spatial, angular (*21, 22*), or correlations in the orbital angular momentum (OAM) (*23, 24*). Building on these foundational insights, advancing a deeper understanding of the underlying mechanisms of light–matter interactions in complex scattering media remains essential for appropriate selection of sensing metrics, probing states, and consequently improving polarization-based sensing and imaging.

Motivated by the quest for improved performance of photonic sensing and imaging, employment of quantum light has already enabled groundbreaking achievements such as sub-shot-noise imaging with two-photon correlated states (*25*), superb phase measurement sensitivity with squeezed states (*26*), or imaging with photons never interacting with the sample (*27*). Among developments toward quantum-enhanced polarimetry

Read at the publisher: https://doi.org/10.1002/lpor.202501172

(*28*) one should mention, e.g., revisiting of quantum polarization theory (*29–31*), experimental realization of nonlocal, or ghost, polarimetry (*32, 33*), and demonstration of sensitivity enhancement in measurements with NOON states (*34–36*). Particularly attractive states are polarization-entangled photons, which find extensive interest in quantum sensing and communication (*37–39*). Especially in the field of biomedical diagnostics, such states hold potential benefits due to the possibility of entanglement preservation through a scattering medium (*40*), deeper penetration of such states into a biological tissue (*41*), and quantitative imaging of biological samples with polarization-entangled photons (*37*). Targeting at practice-oriented solutions, scenarios with decreased number of measurements per sample appear promising. Sensing with Bell states without full quantum process tomography (*42*) proved applicable to monolayer cell cultures (*43*), diluted solutions of microorganisms (*44*), and morphological changes in brain tissue due to Alzheimer's disease (*45, 46*), while holding the potential of enhanced precision of the measurement (*47*) and polarization-based classification with only two coincidence measurements (*48, 49*).

Despite recent advances, quantum polarimetry remains in the early stages of development. Achieving real-world, quantitative diagnostics of complex samples — such as biomedical tissues or other turbid environments — critically depends on a comprehensive understanding of the mechanisms governing the evolution of non-classical light upon interaction with matter, which is yet to be achieved.

A fundamental understanding of how the parameters of non-classical states — most notably their degree of entanglement — are influenced by the optical properties of the medium remains elusive. Moreover, predictive models capable of describing the interaction of such states with complex scattering environments are still lacking. At the same time, such knowledge is crucial for the informed selection of non-classical states tailored to specific tissue types, for the unambiguous interpretation of measured state alterations in terms of tissue optical properties, and for advancing quantitative quantum polarization–based sensing methodologies. Given the broad use of polarization-entangled photons, exploring their behavior in complex media is of particular significance (*50–54*). Predictive insight into how probing photonic states respond to the optical characteristics of a sample is a prerequisite for defining optimal measurement configurations and establishing reliable diagnostic metrics.

In response to the need for such understanding and development of appropriate predictive models, in this work we focus on biomatter–light interaction and explore the evolution of polarization-entangled photons propagating through a turbid medium. For experimental investigations we rely on the acknowledged method of quantum state tomography (QST) (*55*) and analyze the changes of the Bell state after one of the partner photons passes through tissue-mimicking phantoms used as test samples. The latter allow controllable realization of turbid environments with adjustable scattering parameters and imitate closely the

Read at the publisher: https://doi.org/10.1002/lpor.202501172

optical properties of real biomedical samples (*56, 57*). In particular, we reveal a clear dependency of the quantum state on the scattering coefficient of the samples. In our theoretical studies, we target at fundamental understanding, interpretation and prediction of the behavior of the probing quantum state upon interaction with turbid samples. For this, we elaborate on the foundational mathematical relationship between Wolf's coherency matrix (*58, 59*) and the density matrix of the quantum state (*55, 60*). Our proposed treatment of polarization-entangled states paves the way for application of the well-developed classical light scattering approaches to scenarios involving entangled photon states, beginning with those where quantum interference effects within one optical channel can be considered negligible. Particularly, for numerical experiments we employ Monte Carlo (MC) modeling of the photon transfer in turbid media based on the radiative transfer theory for photon propagation (*61*) and the Bethe-Salpeter equation for polarization state tracking of light attenuated by the turbid medium (*62–64*). Hereby, we introduce a direct approach to evaluating Wolf's coherency matrix both for single photons and for photon ensembles (*15*). Our theoretical findings correlate well with experimental observations while allowing to expand the analysis to diverse input states. We not only confirm the clear dependency of the probing state evolution on the scattering properties of the samples, but also reveal the robustness of such trend for different degrees of entanglement of the input state. This, in turn, underscores the potential of quantum polarization-based sensing for quantitative diagnostics in applications ranging from biomedical studies to quantum communication and remote sensing.

Results

In the current study, we consider the light-matter interaction scenario which is schematically visualized in Figure 1. Two photons propagate in separate distant channels. Each photon is either in the horizontal $|H\rangle$ or vertical $|V\rangle$ polarization state, which in terms of the appropriate creation operator $\hat{a}^{\dagger}$ acting on the vacuum state $|0\rangle$ can be defined as $|H\rangle = \hat{a}_H^{\dagger}|0\rangle$ and $|V\rangle = \hat{a}_V^{\dagger}|0\rangle$, correspondingly (*59*). One of the channels contains a sample medium under study where scattering and attenuation of light occur, while another channel remains undisturbed and no loss of photons or change of their state takes place. The photons may be entangled in polarization, and thus the quantum state of the photon pair is evaluated via polarization QST, see "Materials and Methods" section. As an example, we focus on a Bell state in the form $1/\sqrt{2}\,(|HV\rangle + |VH\rangle)$). For the latter, the described scenario means that both $|H\rangle$ and $|V\rangle$ photons can be observed in each channel with equal probability. $|HV\rangle$ state means that the horizontally polarized photon $|H\rangle$ propagates in the first channel containing the scattering sample, while vertically polarized photon $|V\rangle$ propagates through the second, reference channel (undisturbed channel, air environment). The $|VH\rangle$ state is interpreted in a similar manner.

Read at the publisher: https://doi.org/10.1002/lpor.202501172

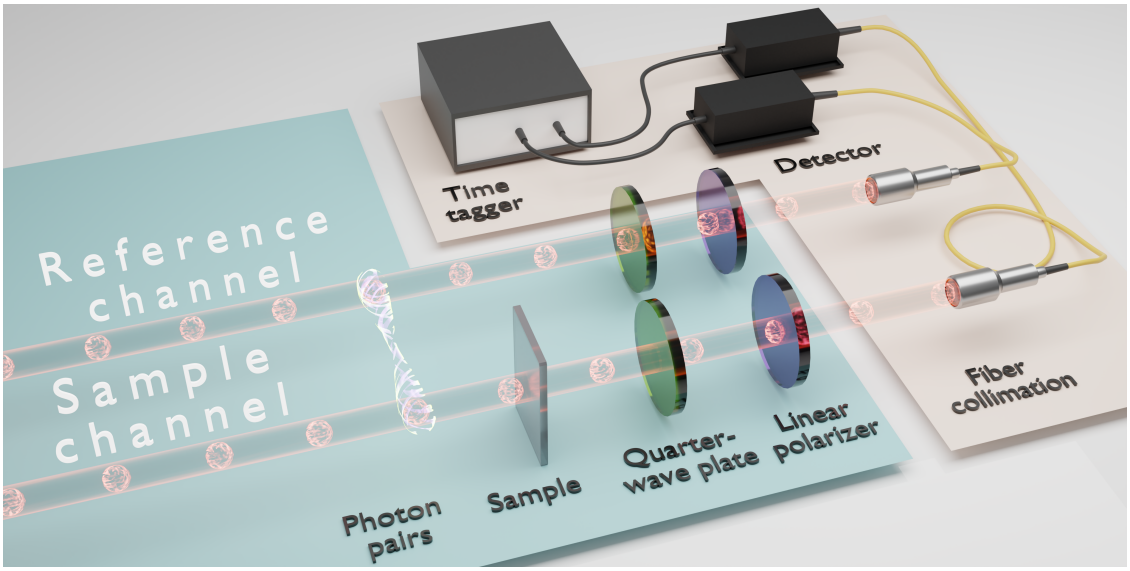

Figure 1: **Studied scenario of polarization-entangled photons scattering in a turbid medium.** One of the photons of polarization-entangled photon pair interacts with a turbid sample. Another photon remains unchanged. Quarter-wave plates and linear polarizers enable polarization projective measurements. Coincidences between the channels upon photon detection are used for two-photon state reconstruction (Materials and Methods).

Theoretical description of multi-photon polarization states

For comprehensive treatment of scattering of polarization-entangled photonic states in complex media consideration of both the classical framework for the description of polarized light (*65*) and the quantum framework for the description of quantum photonic states (*59*) is required. In particular, we propose to investigate the applicability of light scattering models well-developed within the classical electromagnetic theory, to the case of entangled photon scattering. For this, we use Jones and Stokes approaches for polarized light description and Dirac formalism for the description of photon states, bridging these two approaches via concepts of coherency and density matrices. In the following, we use the Jones vector $\boldsymbol{\varepsilon} = (E_x, E_y)^T$ which fully defines the electric field vector $\mathbf{E} = (E_x, E_y, 0)^T$ and therefore allows to describe any polarization state of the fully polarized light. Here and onward, T corresponds to the matrix transpose. By fully polarized state of light we explicitly mean that strict equality holds in the following relation between elements of Stokes vector $\mathbf{S} = (S_0, S_1, S_2, S_3)^T$: $S_0^2 \geq S_1^2 + S_2^2 + S_3^2$. In turn, partially polarized state of light corresponds to the inequality in this expression. Both fully and partially polarized light states can be equivalently described by Wolf's coherency matrix $\mathbf{J}$ (*58*).

The concept of the coherency matrix has been previously linked to the density matrix of a quantum state

Read at the publisher: https://doi.org/10.1002/lpor.202501172

of a single photon (*59*). Stokes parameters, in turn, have been related both to the quantum state of a single photon and generalized to multi-photon states (*55*). In this work, we further elaborate on this connection. As a starting point, we emphasize that in the current context a pure single photon state can be equivalently described both by the Jones vector and by the wavefunction of the quantum state:

$$\boldsymbol{\varepsilon} = \begin{pmatrix} E_x \\ E_y \end{pmatrix} \rightarrow \begin{pmatrix} \psi_1 \\ \psi_2 \end{pmatrix} = |\psi\rangle \tag{1}$$

Here, $|\psi\rangle$ is a pure quantum polarization state of an individual photon. The important difference between the two descriptions resides in the fact that the wavefunction of a quantum state describes probability amplitudes, while the Jones vector describes the electric field. By using an arrow sign we point out that there exists a surjective relation which connects electric field components to the corresponding probability amplitude values. This connection is manifested through the relationship between coherency matrix $\mathbf{J}$ and density matrix $\hat{\rho}$ of the quantum state: $\hat{\rho} = \mathbf{J}/\mathrm{tr}\,(\mathbf{J})$. Here, $\mathrm{tr}(\cdot)$ corresponds to the matrix trace. The derivation of this relationship is quite straightforward with employment of the Dirac ket $|\cdot\rangle$ and bra $\langle\cdot| = \left(|\cdot\rangle^T\right)^*$ vectors defined in the Hilbert and conjugated Hilbert spaces, respectively: coherency matrix of the fully polarized light equals $|\boldsymbol{\varepsilon}\rangle\langle\boldsymbol{\varepsilon}|$ (*65*), which fully coincides with the definition of a density matrix of the pure quantum state $|\psi\rangle\langle\psi|$ (*60*) except for the different scale of coherency matrix due to the presence of complex field amplitudes.

The relationship between $\hat{\rho}$ and $\mathbf{J}$ holds both for pure and mixed states (*55, 59*). As a consequence, fully polarized states of light can be described both by Jones vector and coherency matrix, which corresponds to the pure quantum states of single photons that can be described both by wavefunction and density matrix. In turn, partially polarized states of light can be described only by coherency matrix, and they correspond to mixed quantum states which can be described only by means of the density matrix. Most importantly for the current work, the outlined connection between $\hat{\rho}$ and $\mathbf{J}$ enables to interpret MC models which address single photon scattering (*15*) in terms of quantum states and probability amplitudes.

The Dirac bra-ket framework can be naturally expanded to describe state $|\Psi\rangle = |\psi^{(1)}\rangle \otimes |\psi^{(2)}\rangle = |\psi^{(1)}\rangle|\psi^{(2)}\rangle = |\psi^{(1)}\psi^{(2)}\rangle$ of a separable pair of photons (*55*), where $|\psi^{(i)}\rangle = \left(\psi_1^{(i)}, \psi_2^{(i)}\right)^T$ corresponds to the pure state of a single photon defined according to Eq. (1), and $\otimes$ is a tensor product. For polarization-entangled photon pairs, the state of such system cannot be decomposed into states of separate photons. Pure two-photon polarization-entangled states in the *H*-*V* basis are Bell states: $|\Phi^{\pm}\rangle = \frac{1}{\sqrt{2}}(|HH\rangle \pm |VV\rangle)$, $|\Psi^{\pm}\rangle = \frac{1}{\sqrt{2}}(|HV\rangle \pm |VH\rangle)$. Specifically here, $|H\rangle = (1,0)^T$ and $|V\rangle = (0,1)^T$. In this work, we propose to define such pure states within the Jones-like formalism, allowing to bridge both approaches. In particular, for the

Bell state $|\Psi^+\rangle$ we construct the following equivalent:

$$\mathcal{E} = \frac{1}{\sqrt{2}}\left(\boldsymbol{\varepsilon}_H \otimes \boldsymbol{\varepsilon}_V + \boldsymbol{\varepsilon}_V \otimes \boldsymbol{\varepsilon}_H\right) \rightarrow |\Psi^+\rangle = \frac{1}{\sqrt{2}}(|HV\rangle + |VH\rangle) \tag{2}$$

Here, the Jones vectors of horizontally $\boldsymbol{\varepsilon}_H = (1,0)^T$ and vertically polarized light $\boldsymbol{\varepsilon}_V = (0,1)^T$ are used. In this specific case, they are mathematically equal to $|H\rangle$ and $|V\rangle$ states, but in the general case they can differ by a scale factor related to the light intensity. As in Eq. (1), the arrow denotes the correspondence between the components of $\mathcal{E}$ and the respective elements of $|\Psi^+\rangle$ which ultimately obeys the indicated relationship between $\hat{\rho}$ and $\mathbf{J}$. Vector $\mathcal{E}$ can be used to construct an equivalent to the coherency matrix for a pair of photons $|\mathcal{E}\rangle\langle\mathcal{E}|$, similarly to how expression $|\Psi^+\rangle\langle\Psi^+|$ produces a density matrix of the corresponding Bell state.

In the considered study scenario, one of the partner photons is scattered and therefore acquires a new polarization state. Expressing the selected input Bell state in terms of the creation operators $|\Psi^+\rangle = 1/\sqrt{2}\,(|HV\rangle + |VH\rangle) = 1/\sqrt{2}\left(\hat{a}_H^\dagger|0\rangle|V\rangle + \hat{a}_V^\dagger|0\rangle|H\rangle\right)$ allows to write down a representation for the evolved scattered state (superscript S) in terms of probability amplitudes $\alpha_H, \alpha_V, \beta_H, \beta_V$ obeying $|\alpha_H|^2 + |\alpha_V|^2 = 1,\ |\beta_H|^2 + |\beta_V|^2 = 1$:

$$|\Psi^S\rangle = \frac{1}{\sqrt{2}}\left(\alpha_H\hat{a}_H^\dagger|0\rangle|V\rangle + \alpha_V\hat{a}_V^\dagger|0\rangle|V\rangle + \beta_H\hat{a}_H^\dagger|0\rangle|H\rangle + \beta_V\hat{a}_V^\dagger|0\rangle|H\rangle\right) \tag{3}$$

We do not use the creation operator to expand polarization states in the second channel, since this channel does not contain scattering medium and the corresponding probability amplitudes are assumed not to change. In terms of the proposed Jones-like formalism, this expression takes the form:

$$\mathcal{E}^S \propto \mathfrak{m}\boldsymbol{\varepsilon}_H \otimes \boldsymbol{\varepsilon}_V + \mathfrak{n}\boldsymbol{\varepsilon}_V \otimes \boldsymbol{\varepsilon}_V + \mathfrak{p}\boldsymbol{\varepsilon}_H \otimes \boldsymbol{\varepsilon}_H + \mathfrak{q}\boldsymbol{\varepsilon}_V \otimes \boldsymbol{\varepsilon}_H \rightarrow |\Psi^S\rangle \tag{4}$$

It means that, once we are able to determine the polarization state of a scattered partner photon by means of, e.g., Monte Carlo modeling, then, by conducting proper averaging procedures over the numerous simulated polarization states, it is possible to extract the unknown coefficients $\mathfrak{m}, \mathfrak{n}, \mathfrak{p}, \mathfrak{q}$ and relate them to the probability amplitudes $\alpha_H, \alpha_V, \beta_H, \beta_V$. When there is no scattering medium in the sample channel, coefficients become $\mathfrak{m} = 1, \mathfrak{n} = 0, \mathfrak{p} = 0, \mathfrak{q} = 1$ and expression (4) reduces to the Bell state $|\Psi^+\rangle$ accurately up to a multiplier. It is important to note that if both partner photons are scattered inside the same turbid medium, quantum correlations which can lead to quantum interference effects will have to be taken into account (*54*).

Employing the MC model to evaluate these coefficients is justified by its ability to reveal how the parameters defining the turbid medium influence polarimetric measurement data (*15, 66*), in turn enabling the solution of applied diagnostic tasks (*6, 16*). Details on the proposed generalized MC model, including polarization state tracking and ensemble averaging, are provided in the "Materials and Methods" section.

Read at the publisher: https://doi.org/10.1002/lpor.202501172

Effect of the turbid medium on the Bell state

To explore the scattering of polarization-entangled states in a turbid medium experimentally, we implemented the scenario from Figure 1 in practice. As media under study, we aimed to use real complex samples that would be relevant for biomatter-light interaction. For this reason, we selected tissue-mimicking phantoms that can be manufactured with well-controllable predefined scattering properties. We performed QST both before and after interaction of the probing Bell state with the samples. The reconstructed density matrices $\hat{\rho}$ were analyzed as a whole to observe the global change of the probing state and to retrieve quantitative parameters of the sample affected state. In particular, we considered concurrence C, linear entropy E, purity P, and dephasing expressed as $|\hat{\rho}_{3,2}|$. The scattering properties of the tissue phantoms have been selected to represent a broad range of turbid media, from rather transparent to the opaque. For this, the samples were manufactured with varying scattering coefficient μ_s and other parameters were kept the same. For representation of samples' scattering properties independent of the probed volume, in the following we employ the characteristics of the effective thickness d/l^* defined by the actual thickness of the sample d and photon transport mean free path $l^* \sim \mu_s^{-1}$ (*67*). Further details on samples and experiment realization are given in the "Materials and Methods" section.

A representative measurement outcome, intended to illustrate the obtained density matrix data used for further analysis, is shown in Figure 2. It corresponds to the sample with the highest d/l^* measured within this study (≈ 1.0) and whose optical properties are close to those exhibited by real biological tissues, e.g., human epidermis and dermis (*68*). In particular, interaction of the Bell state with the sample resulted in the transfer of coherencies between $|HV\rangle$ and $|VH\rangle$ basis states (anti-diagonal elements of $\hat{\rho}$) to the imaginary part and decrease in their absolute values as a signature of state decoherence. We accompany the measured matrix with its simulated counterpart which supports the experiment. Moreover, our approach allows to interpret the observed effect as mainly guided by dephasing with a phase delay of $\lambda/14$ arising between $|V\rangle$ and $|H\rangle$ photons. The latter can be explained by a combination of the impact of the birefringence of the samples at the level negligible for classical characterization and the difference of optical paths for $|V\rangle$ and $|H\rangle$ photons accumulated due to multiple scattering events. The dephasing of the state is more pronounced in the simulated output state where also corner elements attain values slightly exceeding the noise level. They attract probabilities from the core elements of $\hat{\rho}$ which suggests the appearance of multiple superposition states with different phase relations. In the Supplementary Material we provide additional explanations on how our interpretations were obtained and the sample-related impact is separated from the phase delays that might be induced by other optics in the light path.

Read at the publisher: https://doi.org/10.1002/lpor.202501172

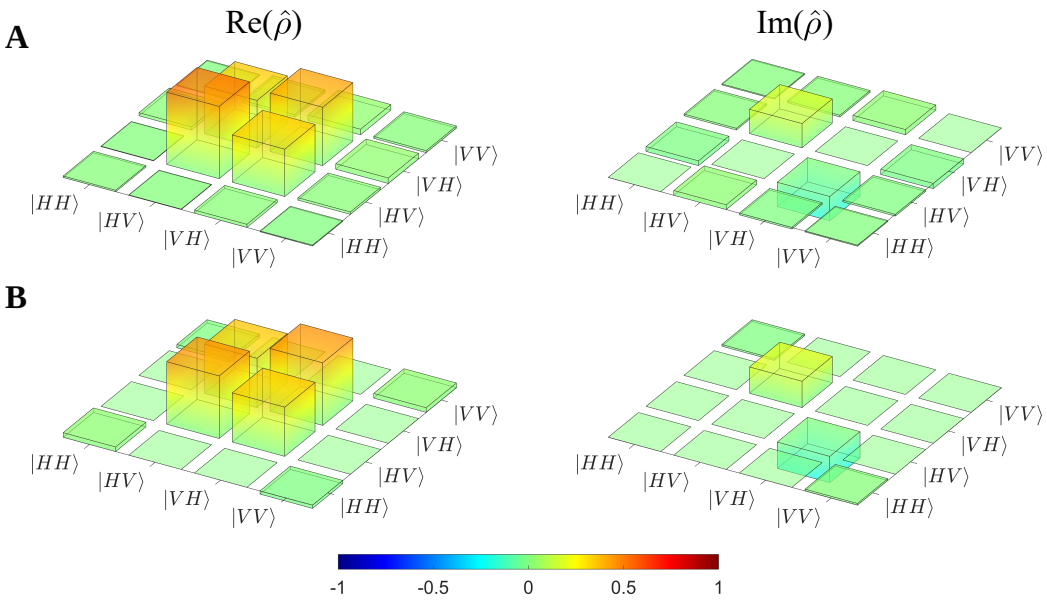

Figure 2: **Observation of the Bell state alteration due to propagation through a dense turbid medium**. Real and imaginary parts of the density matrix of the two-photon state after interaction of one of its partner photons with ZnO-based tissue phantom of $d/l^* \approx 1.0$ in one of the arms: **A** experimentally measured and **B** computed with Eq. (12) with account for the initial state impurity. Simulation parameters are selected to be identical to the measured sample's properties. Theoretical estimate also includes a fit for phase delay equal to $\delta = -\lambda/14$. The obtained fidelity between the measured and simulated matrices is 91%.

For quantitative comparison (Figure 3), we represent the same density matrices reshaped as vectors and supplemented with the error estimation for experimental data as per Ref. (*55*). Here, one can notice that the relative amplitudes for the populations of $|HV\rangle$ and $|VH\rangle$ basis states (core diagonal elements, $\hat{\rho}(6)$ and $\hat{\rho}(11)$) remain balanced in the simulated matrix in contrast to the experiment outcome. This can, though, be attributed to the probable residual differences between the real probing state and its fitted representation used in simulations (Materials and Methods). Nevertheless, as we show next, this has no significant impact on the integral metrics of the quantum state which could be potentially used as diagnostics criteria or monitoring parameters for quantitative sensing. The values of these metrics for both the measured and calculated state lie in close vicinity for the provided example, as well as for other measured tissue phantoms. Further details on the behavior of the density matrix elements discussed above, along with an interpretation of the observed dynamics for the specific case studied here, are provided in the Supplementary Material (Figure S1). More general relationships – particularly those connecting to classically observed polarization measures – could potentially be revealed by exploring a broader range of probing states.

Read at the publisher: https://doi.org/10.1002/lpor.202501172

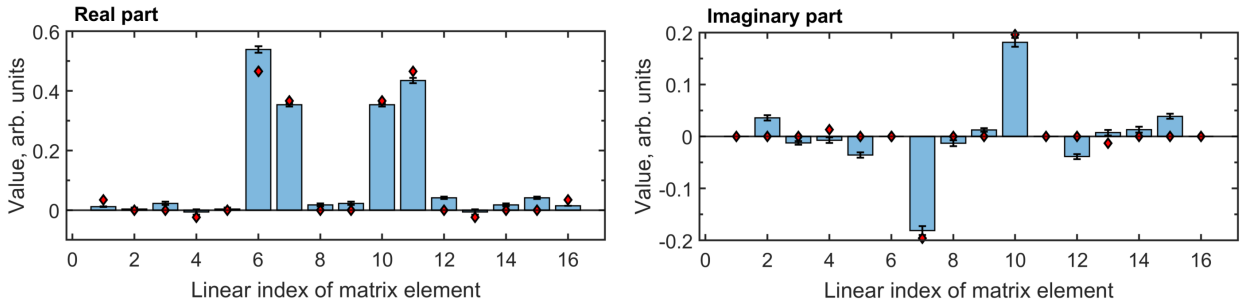

Figure 3: **Correlation between measured and modeled changes to the probing Bell state after interaction with a turbid sample**. Measured (barplot) and modeled (diamonds) density matrix elements from Figure 2 reshaped to vectors. Error bars represent the error estimation as per Ref. (*55*).

Figure 4 summarizes our systematic exploration of the dependency of the probing Bell state on the scattering coefficient of the turbid medium. We demonstrate here dependencies of C, E, P, and $|\hat{\rho}_{3,2}|$ retrieved from experimentally measured and simulated density matrices. In the numerical studies, we expanded the range of the probing states beyond the experimentally realized conditions. The corresponding results are shown with shaded stripes and provide an overview of the MC prediction of the output state dependent on the initial quality (degree of entanglement) of the probing state. In particular, the results are shown for probing states of concurrence C_{pr} = 1.00, 0.95, 0.90, 0.85, 0.80, 0.75, and 0.70. These states were generated via decomposition into basis Bell states (Materials and Methods) with the probability weight factors for $|\Psi^+\rangle$ and $|\Psi^-\rangle$ equal to: $[1, 0]$, $[39/40, 1/40]$, $[19/20, 1/20]$, $[37/40, 3/40]$, $[9/10, 1/10]$, $[7/8, 1/8]$ and $[17/20, 3/20]$. Here, the probability factors for $|\Phi^+\rangle$ and $|\Phi^-\rangle$ have been assumed equal to zero.

In the experiments, the probing state has been prepared with concurrence (0.88±0.01). Such conditions have been simulated assuming the probing state of 0.90, which was found to be fitting best to the experimental data. The fidelities between the measured and simulated density matrices for all samples studied have been obtained in the range from 91% to 98%. Considering the inevitable presence of experimental error and minimal discrepancy between the practically generated probing state and its simulated counterpart, the results demonstrate excellent agreement. For all studied metrics, which reflect both the overall properties of the state (concurrence, entropy, purity) as well as direct monitoring of one of the core elements of the density matrix (dephasing), the modeling and experiment correlate with high accuracy.

Read at the publisher: https://doi.org/10.1002/lpor.202501172

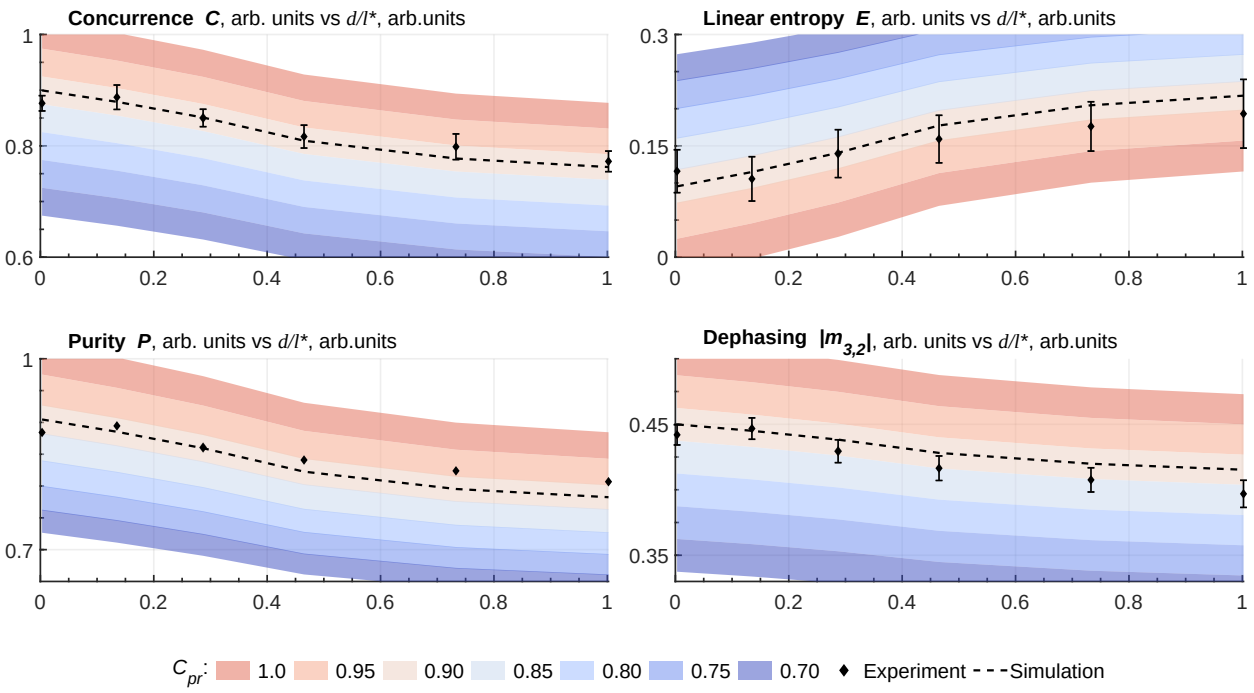

Figure 4: **Evolution of the polarization-entangled two-photon state due to interaction with a scattering medium**. Dependencies of the output state's concurrence, linear entropy, purity, and dephasing vs the effective thickness of the scattering medium d/l^*. Experimentally measured points (diamonds, $C_{pr} = 0.88 \pm 0.01$) with error estimation (*55*) and simulated outcome with best fitting probing state (dashed line, $C_{pr} = 0.90$) for d/l^* = 0.003, 0.135, 0.287, 0.465, 0.733, and 1.002. Shaded stripes show simulation results beyond experimentally realized conditions with different degree of entanglement of the initial probing state C_{pr}= 1.0, 0.95, 0.90, 0.85, 0.80, 0.75, and 0.70.

Discussion

The presented results reveal a clear trend of the state evolution for slow loss of entanglement when one of the partner photons passes through a scattering medium. Moreover, we show that this holds valid for different degrees of entanglement of the initial state incident on the sample, as predicted with our proposed theoretical approach. The non-ambiguous dependence of the entangled state on the scattering properties of the sample – particularly the reduced scattering coefficient – and robustness of the trend to the initial quality of the probing state underscore its diagnostic potential and showcases the monitoring of the state evolution as a robust metric for prospective quantitative characterization of real complex media to be inspected or detected.

The minimal discrepancy between the simulated and experimentally reconstructed states in terms of relative amplitudes for the populations of $|HV\rangle$ and $|VH\rangle$ basis states discussed in the previous section can

Read at the publisher: https://doi.org/10.1002/lpor.202501172

be further improved by more precise matching of the simulated input state to the state actually generated in the experiment. This, though, will require a more complex model of the utilized experimental arrangement and we will address this point in our future studies, along with more detailed interpretation of the dynamics of the specific density matrix elements. Nevertheless, the presented findings explicitly demonstrate the applicability of entangled states for studying turbid media and confirm the applicability of classical scattering approaches like MC to problems involving entangled photon states.

The parameters selected for the test set of samples experimentally measured within this study emphasize the applicability of our proposed treatment of the entangled photon scattering for a wide range of applications. On the one hand, we demonstrated the suitability of our polarization-based sensing approach using Bell states for studying samples with scattering coefficients in the range characteristic for real biological tissues, e.g., human epidermis and dermis (*68*). Consistent with previous and recent studies (*41, 45, 46*), the entanglement is preserved on a high level even for samples with the highest reduced scattering coefficient from the test sample set. This makes the findings of this study particularly relevant for low-flux remote photonics for biomedical diagnostics (*36, 37, 47*). On the other hand, samples from the test set with relatively low scattering coefficients correspond to the properties of various atmospheric conditions, including air polluted with particulate matter or containing water aerosols (*4*). This, in turn, highlights the significance of our proposed method also for applications in precise remote environmental monitoring, optical communication link maintenance, and reliable quantum optical data transmission (*69, 70*).

The particular significance of this study for further development of quantum technologies lies in the inherent scalability of the introduced modeling approach to simulation of multi-photon problems. Numerically, it is possible to introduce the same scattering medium in the second channel of the discussed experimental scenario in a relatively straightforward way. With the cost of increased computational efforts, one can obtain statistically significant amount of possible trajectories of the photons in both channels and for both $|H\rangle$ and $|V\rangle$ states. Applying the analytical description of our model the prediction of the output state in this case would similarly arrive at finding the unknown probability amplitudes. However, it would be necessary to account here also for coherent interactions between the substates of the decomposition (*54*). In addition, the introduced model can be expanded to multi-photon polarization-entangled states. Benefiting from the BSE framework allowing for tracking different polarization states for each single trajectory of the MC photon (Materials and Methods), we have shown the capabilities of the model on example of a two-photon Bell state in the $|H\rangle$ and $|V\rangle$ basis. It is, though, possible to track also other types of initial polarization states, as well as one can consider several spatial channels of photon propagation and not necessarily only two.

In summary, our experimental results reveal a robust dependence of polarization-entangled photons on

the scattering properties of the propagation medium. Combined with our theoretical approach for modeling the scattering of such states in turbid media, these findings deepen the fundamental understanding of photon–medium interactions, enable accurate interpretation, and allow prediction of their outcomes. Beyond advancing fundamental knowledge, our work lays the foundation for establishing optimal scenarios for quantitative sensing with non-classical light, exploring the limits of quantum-enhanced polarization-based sensing, and enabling a broad range of photonic applications that leverage emerging quantum technologies.

Materials and Methods

Samples

As samples of turbid medium with different scattering properties we used in-house manufactured tissue-mimicking phantoms – polymer films with scattering centers (nanoparticles) homogeneously allocated within their volume (*57*). Scattering properties of such phantoms are controlled by the material of scattering centers, their size and distribution profile. For the reported studies, we manufactured a series of thin ($d = 300\ \mu$m thick) tissue phantoms (20 mm × 70 mm) with similar refractive index $n = 1.47$, low absorption coefficient $\mu_a \sim 0.1\ \text{mm}^{-1}$, and forward scattering anisotropy factor $g \approx 0.65$, but with varying density of ZnO nanoparticles acting as scattering centers. The latter resulted in different scattering coefficient μ_s. To account for the impact of g, we characterized samples with the reduced scattering coefficient μ_s' and the transport mean free path l^*, which considering the low level of absorption of the samples can be related as $l^* = 1/\mu_s' = \mu_s^{-1}\,(1-g)^{-1}$ (*67*). Actual values of μ_s' for the measured samples were 0.45, 0.96, 1.55, 2.44, and 3.34 mm^{-1}. Hereby, the effective thickness d/l^* of the samples, which allows for volume-independent scattering characterization, gradually reaches 1.0, while the complete set of samples represents turbid media with scattering relatively low as for polluted air (*4*) to high as for human tissue (*68*). For handling, each sample is mounted between two standard glass microslides. As a reference sample, we use a polymer matrix without ZnO nanoparticles and thus characterized by negligible scattering coefficient.

Probing state generation

The targeted probing quantum state is the Bell state in the form $|\Psi^+\rangle = 1/\sqrt{2}(|HV\rangle + |VH\rangle)$. This state was chosen as it represents one of the most established and widely utilized forms in studies of quantum-enhanced photonic sensing and in quantum communication. It is generated with the source reported in Ref. (*71*) in type-II phase matching configuration. The source employs two identical periodically-poled KTP (Potassium Titanyl Phosphate) crystals, each serving for generation of a pair of orthogonally polarized photons within a

Read at the publisher: https://doi.org/10.1002/lpor.202501172

type-II event of spontaneous parametric down-conversion (SPDC). These crystals are introduced with their optical axes oriented orthogonally into a polarization Mach-Zehnder interferometer and the optical paths of the generated photon pairs are matched to achieve indistinguishability (*72*). The wavelength-degenerate pairs are created at 810 nm, exit the interferometer and the resultant biphoton state is characterized using QST (*55*). The fidelity of the realized state with respect to the nominal Bell state is obtained at the level of 0.97 by proper control of the spatial and temporal walk-off between the beams (*71, 73*). The described source is omitted in Figure 1.

Measurement instrument

Experimental setup for quantum state characterization follows the conceptual visualization in Figure 1. Here, each optical channel contains a polarization projector (or polarization state analyzer) and a fiber-coupled single photon counting module (detector). The polarization projectors are realized with quarter-wave plates (QWP) and linear polarizers (LP) and enable projection to horizontal $|H\rangle$, vertical $|V\rangle$, diagonal $|D\rangle$ (+45°), antidiagonal $|A\rangle$ (-45°), right- $|R\rangle$ and left- $|L\rangle$ circular basis states. For each of these projective measurements, both QWP (with its fast axis) and LP (with its transmission axis) are oriented at appropriate angles with respect to the global vertical direction. The transmitted photons are guided to the detector using a single-mode fiber with numerical aperture of 0.13. The detectors in both channels are connected to a time tagging device for counting the coincidence events. These correspond to the photon pairs reaching the detectors within a narrow time window (coincidence window) which relates these photons to the same SPDC event. Providing the comparable level of coincidences is counted for different independent polarization bases, one can claim them entangled. The samples under study were introduced into one of the optical channels (signal, or sample) without extra condenser or objective lens, so that samples are illuminated with a collimated beam of approx. 1 mm. On the one hand, this allows to probe a relatively large area of the homogeneous phantom and thus obtain an integral response from the sample and extra minimize the influence of any contamination of the sample or localized artifacts. On the other hand, we thus ensure that all the probing photons enter the turbid medium under study at normal incidence and the angular dependence of the polarization effects, also in simulations, can be neglected. At the same time, we introduced an auxiliary (the same for all samples) low-focusing lens between the phantom and polarization projector in the signal channel to enhance the coupling of the scattered photons to the single-mode-fiber input of the detector. The corresponding effective acceptance angle of the detection system (accounting for numerical aperture of the fiber itself) is considered when modeling the experimental conditions with Monte Carlo approach.

Read at the publisher: https://doi.org/10.1002/lpor.202501172

Measurement procedure, data acquisition and processing

To study the effect of the turbid samples on the entangled photons, we sequentially characterized the probing state, output state after the photons in the signal channel are passing through the auxiliary lens only, and the state carrying the information of both the lens and a sample. For this, we performed complete tomographic reconstruction of each mentioned state via QST with 16 combinations of polarization projections and one detector per channels as per Ref. (*55*). The latter included maximum likelihood estimation method (*74*) and similar corrections as in Ref. (*75*).

The measurement procedure was automated using a custom-written MATLAB program for synchronization of the movement of the rotational motors for QWPs and LPs in polarization projectors with the acquisition of the data from the time tagging device. With this, the raw coincidence counts accumulated for 10 s have been retrieved for each polarization projection combination for 3 ns coincidence window, in a sequential manner. The raw data was then corrected for accidental counts, intensity drift, and detector efficiency (*74*).

Decomposition of probing mixed states into basis Bell states

Mixed states can be treated as superposition of pure states in the Bell basis with the appropriate probability amplitudes. The density matrix of a mixed state of polarization-entangled photon pair can be decomposed into a combination of density matrices of Bell states, with weight factors indicating probabilities of these states: $\hat{\rho} = p_1|\Psi^+\rangle\langle\Psi^+| + p_2|\Psi^-\rangle\langle\Psi^-| + p_3|\Phi^+\rangle\langle\Phi^+| + p_4|\Phi^-\rangle\langle\Phi^-|$ (*60*). This expression is used to model the experimentally realized probing state and to expand the range of probing states within the numerical studies. In particular, the state with $\hat{\rho} = 19/20|\Psi^+\rangle\langle\Psi^+| + 1/20|\Psi^-\rangle\langle\Psi^-|$ with $C = 0.90$ was found to be best fitting to the experimental state. Notably, solely the transfer of the coherencies between the basis states to the imaginary part of the density matrix does not impact the purity of the state (Supplementary Material).

Monte Carlo model

Within a turbid scattering medium, each photon can follow a plethora of different trajectories defined by the material properties. We simulate these with the MC algorithm which combines aspects of the Bethe-Salpeter equation (*64*) and radiative transfer theory (*61*), in contrast to quantum MC approaches (*76, 77*) which perform wave function sampling. The model is implemented as custom-written program in MATLAB environment with CUDA-accelerated subroutines for efficient tracing of a large amount of photon trajectories. The model operates with medium parameters μ_s, μ_a, g which ultimately depend on the material's internal structure via

concepts of the scattering phase function, corresponding cross-sections and their averaged values obtained by means of statistical electromagnetics (*61*). The algorithm for single photons and its physical background has been extensively covered in our previous works (*15, 62, 78, 79*). Additional details are also provided in Supplementary Material. Importantly, the photons within MC modeling should not be misinterpreted as physical photons, but are rather considered as statistical particles obeying the radiative transfer equation, which has the formal mathematical structure of a kinetic equation describing the particle transport. Thus in this work, the photons within the MC model will be referred to as photon packets, and physical photons will be referred to as photons.

The key steps of our model include: 1) the launch of a large amount ($N_{inc} > 10^9$) of photon packets from the light source; 2) interaction with the sample (see Figure 5 for artistic illustration of different possible scattered trajectories); and 3) collecting the statistics from the $N_{ph} < N_{inc}$ photon packets which arrive at the detector (*15*). Each photon packet is supplied with a statistical weight W_j, $j = [1...N_{ph}]$, which is proportional to its intensity, and with initial polarization state. In this work, we simulate a uniform intensity distribution, which implies a unit initial weight for each photon packet. In the course of propagation through the turbid medium, the statistical weight of each packet is attenuated with respect to the Beer-Lambert law along its trajectory. After launch, a photon packet begins propagation according to the defined initial direction $\mathbf{s}$, which is updated after each scattering event with respect to the scattering phase function, or after an interface collision event with respect to Snell law. Photon packets satisfying the detection conditions are contributing to the final statistics.

Tracing of probability amplitudes

We describe single photon packets by using the relationship (1) and track the evolution of the polarization state of photon packets that undergo scattering and are later detected. For this, we introduce the three-component polarization vector $\mathbf{P}$ which corresponds to the $\mathbf{E}$ field direction (*62, 78–80*). This representation allows to assign any input polarization state to the launched photon packet. Each photon packet trajectory, which contains N scattering events, at start is supplied with a $\mathbf{P}_0$ vector representing its initial polarization state. In case of the $\boldsymbol{\varepsilon}_H$ state $\mathbf{P}_0^H = (1, 0, 0)^T$, and for the $\boldsymbol{\varepsilon}_V$ state $\mathbf{P}_0^V = (0, 1, 0)^T$. Then, within the iterative solution to BSE (*62*), the evolution of this vector can be traced along the photon packet trajectory (*15, 78, 80*):

$$\mathbf{P}_N = \hat{\mathbf{U}}_N \hat{\mathbf{U}}_{N-1} \hat{\mathbf{U}}_{N-2} ... \hat{\mathbf{U}}_1 \mathbf{P}_0, \quad \hat{\mathbf{U}}_i = -\mathbf{s}_i \times [\mathbf{s}_i \times \mathbf{P}_{i-1}] \tag{5}$$

Here, $\mathbf{P}_N$ corresponds to the polarization state of the photon packet that has arrived on the detector and $\mathbf{s}_i$ corresponds to the photon packet direction after the i-th scattering event. With $\mathbf{P}_N$ value obtained, the final

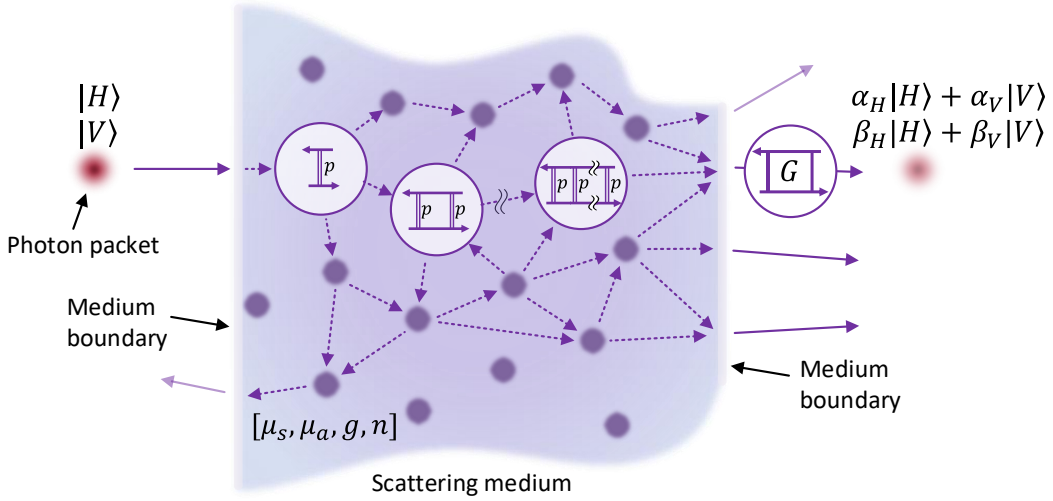

Figure 5: **Schematic representation of possible trajectories of the photon packets passing through a scattering medium.** Notation $|H\rangle$ and $|V\rangle$ addresses the problem of entangled state modeling, where each trajectory can be followed by a photon packet with both horizontal $|H\rangle$ and vertical $|V\rangle$ polarization. In turn, $\alpha_H|H\rangle + \alpha_V|V\rangle$ and $\beta_H|H\rangle + \beta_V|V\rangle$ correspond to the resultant polarization states for initial either $|H\rangle$ or $|V\rangle$ input states. μ_s, μ_a, g, and n define the properties of the medium: scattering coefficient, absorption coefficient, scattering anisotropy factor, and refractive index, correspondingly (*67*). One of the trajectories features ladder diagrams for visualization of the iterative solution of the Bethe-Salpeter equation. Here, G denotes the propagator of the Bethe-Salpeter equation and p stands for the scattering phase function (adapted from Ref. (*62*)).

polarization state of each photon packet can be reconstructed in the form of the Jones vector $\boldsymbol{\varepsilon}$ by switching to a reference frame of the photon packet (*59*). It is important to note that individual photon packets remain fully polarized after each scattering or interface interaction event (*15*). This fact enables application of the Jones formalism to describe polarization state of the scattered photon packets. We also note that this approach works within the Rayleigh-Gans-Debye approximation. The latter assumes that the medium turbidity is conditioned by the presence of optically soft particles in it, which means that the refractive index of each scatterer is close to that of the surrounding medium (*78, 80, 81*). By using $\mathbf{J} = |\boldsymbol{\varepsilon}\rangle\langle\boldsymbol{\varepsilon}|$ and $\hat{\rho} = \mathbf{J}/\mathrm{tr}(\mathbf{J})$, for each photon packet we can obtain the appropriate coherency and density matrices.

The goal of this study is modeling of polarization-entangled photons on the example of a Bell state $|\Psi^+\rangle$. For this reason, we aim to trace possible evolution of both horizontal and vertical polarization states along the same photon packet trajectory. We achieve this by assigning a pair of independent vectors $\mathbf{P}_0^H$ and $\mathbf{P}_0^V$ to each photon packet and tracing them along the same trajectory. This plays an essential role for modeling the

Read at the publisher: https://doi.org/10.1002/lpor.202501172

entangled photons' behavior, since until the detection of one of the partner photons the polarization state of both of them is not defined.

For each j-th photon packet launched with $\mathbf{P}_0^H$ $\left(\mathbf{P}_0^V\right)$ polarization, we denote Jones vector which corresponds to its final polarization state at the detector as $\mathbf{X}_j$ $\left(\mathbf{Y}_j\right)$, and decompose it into the H-V basis components with the weight factors $\mathfrak{m}_j$ and $\mathfrak{n}_j$ ($\mathfrak{p}_j$ and $\mathfrak{q}_j$):

$$\mathbf{X}_j = \mathfrak{m}_j \begin{pmatrix} 1 \\ 0 \end{pmatrix} + \mathfrak{n}_j \begin{pmatrix} 0 \\ 1 \end{pmatrix}, \quad \mathbf{Y}_j = \mathfrak{p}_j \begin{pmatrix} 1 \\ 0 \end{pmatrix} + \mathfrak{q}_j \begin{pmatrix} 0 \\ 1 \end{pmatrix} \tag{6}$$

Hereby, our MC polarization tracing model (5) allows to simulate the behavior of Jones vector expressed via coefficients $\mathfrak{m}_j, \mathfrak{n}_j$ or $\mathfrak{p}_j, \mathfrak{q}_j$ in the scattering medium for any j-th photon packet trajectory. Investigation of the entangled photon pairs is then performed with respect to Eq. (4). In particular, we state that for the considered scenario the unknown probability amplitudes can be extracted from the simulated polarization states described by Eq. (6) by following the Jones-like vector $\mathcal{E}_j$ of a j-th photon packet pair defined in Eq. (2) and assuming that the state of one of the partner photon packets has changed:

$$\begin{aligned} \mathcal{E}_j^S \propto \mathbf{X}_j \otimes \boldsymbol{\varepsilon}_V + \mathbf{Y}_j \otimes \boldsymbol{\varepsilon}_H = \mathfrak{m}_j \boldsymbol{\varepsilon}_H \otimes \boldsymbol{\varepsilon}_V + \mathfrak{n}_j \boldsymbol{\varepsilon}_V \otimes \boldsymbol{\varepsilon}_V + \mathfrak{p}_j \boldsymbol{\varepsilon}_H \otimes \boldsymbol{\varepsilon}_H + \mathfrak{q}_j \boldsymbol{\varepsilon}_V \otimes \boldsymbol{\varepsilon}_H = \\ = \begin{pmatrix} 0 \\ \mathfrak{m}_j \\ 0 \\ \mathfrak{n}_j \end{pmatrix} + \begin{pmatrix} \mathfrak{p}_j \\ 0 \\ \mathfrak{q}_j \\ 0 \end{pmatrix} = \begin{pmatrix} \mathfrak{p}_j \\ \mathfrak{m}_j \\ \mathfrak{q}_j \\ \mathfrak{n}_j \end{pmatrix} \rightarrow \begin{pmatrix} \beta_{Hj} \\ \alpha_{Hj} \\ \beta_{Vj} \\ \alpha_{Vj} \end{pmatrix} \propto |\Psi_j^S\rangle \end{aligned} \tag{7}$$

Here, we strongly rely on the following facts: each photon packet has a pure state after each scattering event, and states $\mathbf{X}_j$ and $\mathbf{Y}_j$ are independently evaluated along the same photon packet trajectory. Expression (7) allows us to construct an equivalent of Wolf's coherency matrix for the pure state of the j-th photon packet pair:

$$\hat{\rho}_j = |\mathcal{E}_j^S\rangle\langle\mathcal{E}_j^S| \rightarrow |\Psi_j^S\rangle\langle\Psi_j^S| \tag{8}$$

To be interpreted as a density matrix, $\hat{\rho}_j$ has to be divided by the trace $\mathrm{tr}(\hat{\rho}_j)$. We again emphasize that if both partner photons are scattered inside the same turbid medium, quantum correlations which can lead to quantum interference effects will have to be taken into account.

Ensemble averaging

Expression (7) is valid for the pure state when a single MC trajectory for the photon packet in the sample channel is considered. In the general case, an ensemble $j = [1...N_{ph}]$ of either photon packets or photon

Read at the publisher: https://doi.org/10.1002/lpor.202501172

packet pairs is considered, resulting in a mixed state. To evaluate the final mixed states, we gather statistics for a significant amount of the detected photon packet pairs and address the question of proper $\hat{\rho}_j$ averaging over the obtained ensemble.

Physically, partially polarized light originates from the field superposition of many light sources with respect to the detector spectral and spatial resolution and finite integration time. In polarimetric biophotonic applications, where individual photon packets with either $\mathbf{X}_j$ or $\mathbf{Y}_j$ detected state are separately considered, one would commonly compute the Stokes vector or, equivalently, 6 intensity values for each photon packet for horizontal (I_H), vertical (I_V), +45° or diagonal (I_D), -45° or anti-diagonal (I_A), right- (I_R) and left- (I_L) circular polarization states and then average them over the whole ensemble of the detected photon packets (*15*). In this work, this averaging can be performed without accounting for coherent effects:

$$I_\phi = \frac{1}{N_{ph}} \sum_{j=1}^{N_{ph}} I_\phi(\mathbf{X}_j) \tag{9}$$

Here, $I_\phi(\mathbf{X}_j)$ is intensity projection of the j-th photon packet with polarization state $\mathbf{X}_j$ on the polarizer state ϕ, and I_ϕ is the ensemble averaged intensity projection. It is necessary to mention that each intensity projection of the photon packet is computed as a product of the polarization state intensity projection $\langle\phi|\mathbf{J}|\phi\rangle$ and two scalar values: statistical weight of the photon packet W and Rayleigh factor Γ_R in the power of number of scattering events $I_\phi(\mathbf{X}_j) = W_j\langle\phi|\mathbf{X}_j\rangle\langle\mathbf{X}_j|\phi\rangle\Gamma_R^{N_j}$ (*79*). Here, W_j is the detected statistical weight of the j-th photon packet which has propagated through the turbid sample, N_j denotes the amount of scattering events along the j-the photon packet trajectory prior to the detection event, $\Gamma_R = 2/\left(1 + \overline{\cos^2\theta}\right)$ is the Rayleigh factor derived from the optical theorem in Born approximation, and $\overline{\cos^2\theta}$ is the square cosine of the scattering angle weighted by the single scattering cross-section (*62, 79*).

In the case of two-photon packets, generalized Stokes parameters or the equivalent density matrix have to be evaluated (*55*). As demonstrated above, in the experiment by a proper selection of the measurement state set the final density matrix $\hat{\rho}$ of the quantum state can be reconstructed (*55, 74, 82*). While direct reproduction of QST can be implemented in the model, it appears to be redundant. Instead, we demonstrate that it is possible to straightforwardly average an equivalent of Wolf's coherency matrix $\hat{\rho}_j$ defined according to Eq. (8) over the ensemble of photon packet pairs thus obtaining a mixed state as a general result. For this purpose, we introduce notation Φ for any allowable state of the photon packet pair and use the associativity property for the product between a vector and the real scalar $W_j\Gamma_R^{N_j}$:

$$I_\Phi(\hat{\rho}_j) = W_j\langle\Phi|\hat{\rho}_j|\Phi\rangle\Gamma_R^{N_j} = \langle\Phi|W_j\hat{\rho}_j\Gamma_R^{N_j}|\Phi\rangle \tag{10}$$

For the ensemble of photon packet pairs, observable intensity projection on the chosen state Φ is then

obtained with the following averaging procedure:

$$I_\Phi \propto \sum_{j=1}^{N_{ph}} I_\Phi(\hat{\rho}_j) = \sum_{j=1}^{N_{ph}} \langle\Phi|W_j\hat{\rho}_j\Gamma_R^{N_j}|\Phi\rangle = \langle\Phi|\left(\sum_{j=1}^{N_{ph}} W_j\hat{\rho}_j\Gamma_R^{N_j}\right)|\Phi\rangle = \langle\Phi|\hat{\rho}_{\text{avg}}|\Phi\rangle \tag{11}$$

Here, we have directly applied the summation over the ensemble of the detected photon packet pairs $j = [1...N_{ph}]$ to the $W_j\hat{\rho}_j\Gamma_R^{N_j}$ term due to the distributivity of the matrix product with respect to the matrix addition, allowing to introduce $\hat{\rho}_{\text{avg}}$: a counterpart of Wolf's coherency matrix for an ensemble of photon packet pairs. As opposed to $\hat{\rho}_j$, this averaged matrix in general corresponds to the mixed state.

With account for the relationship between coherency and density matrices, we obtain the final expression for the simulated density matrix of the two-photon state which is mixed in the general case:

$$\hat{\rho} = \hat{\rho}_{\text{avg}}/\text{tr}\left(\hat{\rho}_{\text{avg}}\right) \tag{12}$$

Such a matrix models the target final two-photon state and thus allows for analysis of the state evolution due to scattering within the turbid medium. Relations (7)–(8) and (10)–(12) are the key expressions of the generalized MC approach and are applied in our numerical experiments.

Read at the publisher: https://doi.org/10.1002/lpor.202501172

References

1. J. Yin, *et al.*, Satellite-based entanglement distribution over 1200 kilometers. *Science* **356** (6343), 1140–1144 (2017).

2. Y. Ren, *et al.*, Atmospheric turbulence effects on the performance of a free space optical link employing orbital angular momentum multiplexing. *Opt. Lett.* **38** (20), 4062–4065 (2013).

3. J. Cao, *et al.*, Robust Optical Quantum Imaging Framework with Entangled Photons in Oceanic Turbulent Environments. *IEEE Trans. Commun.* (2025).

4. A. Marshak, A. B. Davis, eds., *3D Radiative Transfer in Cloudy Atmospheres* (Springer, Berlin) (2005).

5. Z. A. Steelman, D. S. Ho, K. K. Chu, A. Wax, Light-scattering methods for tissue diagnosis. *Optica* **6** (4), 479–489 (2019).

6. V. Periyasamy, M. Pramanik, Advances in Monte Carlo Simulation for Light Propagation in Tissue. *IEEE Rev. Biomed. Eng.* **10**, 125–135 (2017).

7. R. M. A. Azzam, Stokes-vector and Mueller-matrix polarimetry [Invited]. *J. Opt. Soc. Am. A* **33** (7), 1396–1408 (2016).

8. C. He, *et al.*, Polarisation optics for biomedical and clinical applications: a review. *Light Sci. Appl.* **10** (1), 194 (2021).

9. M. Borovkova, *et al.*, Screening of Alzheimer's Disease with Multiwavelength Stokes Polarimetry in a Mouse Model. *IEEE Trans. Med. Imaging* **41**, 977–982 (2022).

10. M. A. Borovkova, A. V. Bykov, A. Popov, I. V. Meglinski, Role of scattering and birefringence in phase retardation revealed by locus of Stokes vector on Poincaré sphere. *J. Biomed. Opt.* **25**, 057001 (2020).

11. A. Lininger, *et al.*, Chirality in Light–Matter Interaction. *Adv. Mater.* **35** (34), 2107325 (2023).

12. F. C. MacKintosh, J. X. Zhu, D. J. Pine, D. A. Weitz, Polarization memory of multiply scattered light. *Phys. Rev. B* **40**, 9342–9345 (1989).

13. D. Bicout, C. Brosseau, A. S. Martinez, J. M. Schmitt, Depolarization of multiply scattered waves by spherical diffusers: Influence of the size parameter. *Phys. Rev. E* **49**, 1767 – 1770 (1994).

14. A. D. Kim, M. Moscoso, Influence of the relative refractive index on the depolarization of multiply scattered waves. *Phys. Rev. E* **64**, 026612 (2001).

15. I. Lopushenko, O. Sieryi, A. Bykov, I. Meglinski, Exploring the evolution of circular polarized light backscattered from turbid tissue-like disperse medium utilizing generalized Monte Carlo modeling approach with a combined use of Jones and Stokes-Mueller formalisms. *J. Biomed. Opt.* **29** (5), 052913 (2024).

16. V. Dremin, *et al.*, Influence of blood pulsation on diagnostic volume in pulse oximetry and photoplethysmography measurements. *Appl. Opt.* **58** (34), 9398–9405 (2019).

17. S. L. Jacques, Optical properties of biological tissues: a review. *Phys. Med. Biol.* **58** (11), R37 (2013).

18. S. Demos, R. R. Alfano, Optical polarization imaging. *Appl. Opt.* **36** (1), 150–155 (1997).

19. C. M. Macdonald, S. L. Jacques, I. V. Meglinski, Circular polarization memory in polydisperse scattering media. *Phys. Rev. E* **91**, 033204 (2015).

20. M. D. Singh, A. Vitkin, Polarized light backscattering from turbid media: why do Rayleigh scatterers preserve linear polarization more than circular polarization? *Laser Photonics Rev.* p. e01487 (2025).

21. S. Feng, C. Kane, P. A. Lee, A. D. Stone, Correlations and Fluctuations of Coherent Wave Transmission through Disordered Media. *Phys. Rev. Lett.* **61**, 834–837 (1988).

22. I. Freund, M. Rosenbluh, S. Feng, Memory Effects in Propagation of Optical Waves through Disordered Media. *Phys. Rev. Lett.* **61**, 2328–2331 (1988).

23. I. Meglinski, I. Lopushenko, A. Sdobnov, A. Bykov, Phase preservation of orbital angular momentum of light in multiple scattering environment. *Light Sci. Appl.* **13**, 214 (2024).

24. F. Khanom, *et al.*, Twists through turbidity: propagation of light carrying orbital angular momentum through a complex scattering medium. *Sci. Rep.* **14** (1), 20662 (2024).

25. N. Samantaray, I. Ruo-Berchera, A. Meda, M. Genovese, Realization of the first sub-shot-noise wide field microscope. *Light Sci. Appl.* **6** (7), e17005–e17005 (2017).

26. Y. Israel, S. Rosen, Y. Silberberg, Supersensitive Polarization Microscopy Using NOON States of Light. *Phys. Rev. Lett.* **112**, 103604 (2014).

27. G. B. Lemos, *et al.*, Quantum imaging with undetected photons. *Nature* **512** (7515), 409–412 (2014).

28. L. Zhang, C. Zou, Y. Wang, F. Setzpfandt, V. R. Besaga, Polarization in quantum photonic sensing [Invited]. *Chin. Opt. Lett.* **23** (11), 092701 (2025).

29. A. F. Abouraddy, A. V. Sergienko, B. E. Saleh, M. C. Teich, Quantum entanglement and the two-photon Stokes parameters. *Opt. Commun.* **201** (1), 93–98 (2002).

30. G. Björk, *et al.*, Quantum degrees of polarization. *Opt. Commun.* **283** (22), 4440–4447 (2010).

31. A. Z. Goldberg, Quantum polarimetry, in *Progress in Optics*, T. D. Visser, Ed. (Elsevier), vol. 67, pp. 185–274 (2022).

32. S. Restuccia, G. M. Gibson, L. Cronin, M. J. Padgett, Measuring optical activity with unpolarized light: Ghost polarimetry. *Phys. Rev. A* **106**, 062601 (2022).

33. S. Magnitskiy, D. Agapov, A. Chirkin, Quantum ghost polarimetry with entangled photons. *Opt. Lett.* **47** (4), 754–757 (2022).

34. F. Wolfgramm, C. Vitelli, F. A. Beduini, N. Godbout, M. W. Mitchell, Entanglement-enhanced probing of a delicate material system. *Nat. Photonics* **7** (1), 28–32 (2013).

35. A. Belsley, J. C. F. Matthews, Estimating the concentration of chiral media with bright squeezed light. *Appl. Phys. Lett.* **121** (18), 184001 (2022).

36. A. Pedram, V. Besaga, L. Gassab, F. Setzpfandt, O. E. Müstecaplıoğlu, Quantum Estimation of the Stokes Vector Rotation for a General Polarimetric Transformation. *New J. Phys.* **26**, 093033 (2024).

37. Y. Zhang, *et al.*, Quantum imaging of biological organisms through spatial and polarization entanglement. *Sci. Adv.* **10**, eadk1495 (2024).

38. T. Ono, R. Okamoto, S. Takeuchi, An entanglement-enhanced microscope. *Nat. Commun.* **4** (1), 2426 (2013).

39. Y. Liu, *et al.*, Quantum integrated sensing and communication via entanglement. *Phys. Rev. Appl.* **22**, 034051 (2024).

40. J. L. van Velsen, C. W. J. Beenakker, Transition from pure-state to mixed-state entanglement by random scattering. *Phys. Rev. A* **70**, 032325 (2004).

41. L. Shi, E. J. Galvez, R. R. Alfano, Photon Entanglement Through Brain Tissue. *Sci. Rep.* **6** (1), 37714 (2016).

42. M. Mohseni, A. T. Rezakhani, D. A. Lidar, Quantum-process tomography: Resource analysis of different strategies. *Phys. Rev. A* **77**, 032322 (2008).

43. L. Zhang, *et al.*, Probing polarization response of monolayer cell cultures with entangled photon pairs. *J. Biophotonics* p. e202400018 (2024).

44. V. R. Besaga, F. Ott, T. Meyer-Zedler, F. Setzpfandt, Application of polarization-entangled photon pairs for studying the density of microorganisms. *Proc. SPIE* **12993**, 129930A (2024).

45. E. J. Galvez, *et al.*, Decoherence of photon entanglement by transmission through brain tissue with Alzheimer's disease. *Biomed. Opt. Express* **13** (12), 6621–6630 (2022).

46. S. Sundar, *et al.*, Discerning Amyloid-β and Tau Pathologies with Learning-Based Quantum Sensing. *ACS Photonics* **12** (10), 5510–5521 (2025).

47. A. Pedram, V. R. Besaga, F. Setzpfandt, O. E. Müstecaplıoğlu, Nonlocality Enhanced Precision in Quantum Polarimetry via Entangled Photons. *Adv. Quantum Technol.* p. 2400059 (2024).

48. A. Vega, T. Pertsch, F. Setzpfandt, A. A. Sukhorukov, Metasurface-Assisted Quantum Ghost Discrimination of Polarization Objects. *Phys. Rev. Appl.* **16**, 064032 (2021).

49. V. R. Besaga, *et al.*, Nonlocal quantum differentiation between polarization objects using entanglement. *APL Photonics* **9** (4), 041301 (2024).

50. J. R. Ott, N. A. Mortensen, P. Lodahl, Quantum interference and entanglement induced by multiple scattering of light. *Phys. Rev. Lett.* **105**, 090501 (2010).

51. M. Candé, A. Goetschy, S. E. Skipetrov, Transmission of quantum entanglement through a random medium. *Europhys. Lett.* **107** (5), 54004 (2014).

52. N. H. Valencia, S. Goel, W. McCutcheon, H. Defienne, M. Malik, Unscrambling entanglement through a complex medium. *Nat. Phys.* **16** (11), 1112–1116 (2020).

53. O. Lib, Y. Bromberg, Quantum light in complex media and its applications. *Nat. Phys.* **18** (9), 986–993 (2022).

54. M. Safadi, *et al.*, Coherent backscattering of entangled photon pairs. *Nat. Phys.* **19** (4), 562–568 (2023).

55. D. F. V. James, P. G. Kwiat, W. J. Munro, A. G. White, Measurement of qubits. *Phys. Rev. A* **64**, 052312 (2001).

56. O. Sieryi, A. Sdobnov, I. Meglinski, A. Bykov, Advanced optical phantom mimicking microvascular and directed blood flow in mouse brain. *Biomed. Eng. Lett.* **15** (2025).

57. O. Sieryi, A. Popov, V. Kalchenko, A. Bykov, I. Meglinski, Tissue-mimicking phantoms for biomedical applications. *Proc. SPIE* **11363**, 1136312 (2020).

58. E. Wolf, Coherence properties of partially polarized electromagnetic radiation. *Nuovo Cim* **13**, 1165–1181 (1959).

59. L. Mandel, E. Wolf, *Optical coherence and quantum optics* (Cambridge University Press, Cambridge) (1995).

60. L. D. Landau, E. M. Lifshitz, *Quantum Mechanics: Non-Relativistic Theory, 3rd edition* (Pergamon Press) (1977).

61. M. I. Mishchenko, Vector radiative transfer equation for arbitrarily shaped and arbitrarily oriented particles: a microphysical derivation from statistical electromagnetics. *Appl. Opt.* **41**, 7114–7134 (2002).

62. I. Meglinski, V. L. Kuzmin, D. Y. Churmakov, D. A. Greenhalgh, Monte Carlo Simulation of Coherent Effects in Multiple Scattering. *Proc. R. Soc. A* **461**, 43–53 (2005).

63. V. Kuz'min, I. Meglinski, Coherent effects of multiple scattering for scalar and electromagnetic fields: Monte–Carlo simulation and Milne-like solutions. *Opt. Commun.* **273** (2), 307–310 (2007).

64. A. Doicu, M. I. Mishchenko, An overview of methods for deriving the radiative transfer theory from the Maxwell equations. II: Approach based on the Dyson and Bethe–Salpeter equations. *J. Quant. Spectrosc. Radiat. Transfer* **224**, 25–36 (2019).

65. M. Born, E. Wolf, *Principles of Optics* (Cambridge University Press) (2019).

66. V. Dremin, *et al.*, Incremental residual polarization caused by aging in human skin. *J. Biomed. Opt.* **29** (5), 052912 (2023).

67. V. V. Tuchin, *Tissue Optics: Light Scattering Methods and Instruments for Medical Diagnostics* (SPIE Press, Bellingham, Washington), 3rd ed. (2015).

68. A. N. Bashkatov, E. A. Genina, V. V. Tuchin, Optical properties of skin, subcutaneous, and muscle tissues: a review. *J. Innov. Opt. Health Sci.* **04** (01), 9–38 (2011).

69. V. Nikulin, *et al.*, Effects of atmospheric turbulence on polarization entanglement in free-space quantum communication links. *Proc. SPIE* **13106**, 131060A (2024).

70. T. Jaouni, *et al.*, Predicting atmospheric turbulence for secure quantum communications in free space. *Opt. Express* **33** (5), 10759–10776 (2025).

71. R. Fazili, *et al.*, Simple but efficient polarization-entangled photon sources. *J. Opt. Soc. Am. B* **41** (12), 2692–2701 (2024).

72. R. Horn, T. Jennewein, Auto-balancing and robust interferometer designs for polarization entangled photon sources. *Opt. Express* **27** (12), 17369–17376 (2019).

73. S. Oh, T. Jennewein, Polarization entanglement with highly nondegenerate photon pairs enhanced by an effective walk-off-compensation method. *Phys. Rev. A* **110**, 063515 (2024).

74. M. Paris, J. Řeháček, eds., *Quantum State Estimation* (Springer Berlin Heidelberg, Berlin, Heidelberg) (2004).

75. M. A. Weissflog, *et al.*, Nonlinear nanoresonators for Bell state generation. *Appl. Phys. Rev.* **11** (1), 011403 (2024).

76. J. Kim, A. T. Baczewski, T. D. Beaudet et al., QMCPACK: an open source *ab initio* quantum Monte Carlo package for the electronic structure of atoms, molecules and solids. *J. Phys. Condens. Matter* **30** (19), 195901 (2018).

77. J. Carlson, *et al.*, Quantum Monte Carlo methods for nuclear physics. *Rev. Mod. Phys.* **87**, 1067–1118 (2015).

78. I. Meglinski, A. Doronin, Monte Carlo Modeling of Photon Migration for the Needs of Biomedical Optics and Biophotonics, in *Advanced Biophotonics: Tissue Optical Sectioning*, R. K. Wang, V. V. Tuchin, Eds. (CRC Press, Boca Raton), chap. 1, pp. 1–72 (2013).

79. V. Kuz'min, I. Meglinski, Numerical simulation of coherent backscattering and temporal intensity correlations in random media. *Quantum Electron.* **36** (11), 990 (2006).

80. E. Akkermans, P. E. Wolf, R. Maynard, G. Maret, Theoretical study of the coherent backscattering of light by disordered media. *J. Phys. France* **49**, 77–98 (1988).

81. C. F. Bohren, D. R. Huffman, *Absorption and Scattering of Light by Small Particles* (Wiley, New York) (1983).

82. E. J. Galvez, *et al.*, Direct measurement of the density matrix of a two-photon polarization qubit. *Proc. SPIE* **12373**, 123730C (2023).

83. Y. Shen, *et al.*, Polarization Aberrations in High-Numerical-Aperture Lens Systems and Their Effects on Vectorial-Information Sensing. *Remote Sens.* **14** (8), 1932 (2022).

Acknowledgments

We would like to thank Prof. Fabian Steinlechner and Mr. Purujit Singh Chauhan for providing the source of polarization-entangled photon pairs and Ms. Luosha Zhang for her help in initial alignment of the measurement system.

Funding: This research has been supported by Horizon 2020 COST Actions: CA23125 – The mETamaterial foRmalism approach to recognize cAncer (TETRA) and CA21159 – Understanding interaction light - biological surfaces: possibility for new electronic materials and devices (PhoBioS). The work has also been partly funded by German Ministry of Education and Research (project ”QUANCER”, FKZ 13N16441), Academy of Finland (grant project 325097) and UK Department for Science Innovation and Technology in partnership with the British Council. V.B. thanks for funding of this work also to ProChance-career program of the Friedrich Schiller University Jena.

Author contributions: V.R.B., I.V.L., F.S. and I.M. conceived the study and developed its concept. V.R.B., I.V.L., A.B., F.S. and I.M. developed methodology. V.R.B. developed experimental approach for polarization-based sensing with two-photon states, realized experimental setup, designed and performed experiments, implemented data acquisition and processing, prepared visualization. I.V.L. developed theoretical framework and generalized MC approach for two-photon states, implemented code, designed and performed numerical simulations. O.S. manufactured and prepared samples for experimental investigation. O.S. and A.B. characterized samples. F.S. provided resources for experimental investigations. I.V.L., A.B. and I.M. developed the polarization tracing MC approach. V.R.B., I.V.L., F.S. and I.M. validated and interpreted results. A.B., F.S. and I.M. supervised the project. V.R.B. and I.V.L. wrote original draft. All authors discussed the results and contributed to reviewing and editing the manuscript.

Competing interests: There are no competing interests to declare.

Data and materials availability: All data needed to evaluate the conclusions in the paper are present in the paper and/or the Supplementary Materials.

Supplementary Materials for
Bridging classical and quantum approaches for quantitative sensing of turbid media with polarization-entangled photons

Vira R. Besaga*†, Ivan V. Lopushenko*†, Oleksii Sieryi, Alexander Bykov,
Frank Setzpfandt, Igor Meglinski

*Corresponding authors. Email: vira.besaga@uni-jena.de and ivan.lopushenko@oulu.fi

†These authors contributed equally to this work.

Appearance of phase retardation effects in the density matrix of a Bell state

Density matrix of the pure Bell state $|\Psi^+\rangle$ is well-known to be a real 4×4 matrix with zero side elements and four central elements equal to 0.5. This corresponds to the case of maximally entangled state characterized by unit concurrence and zero linear entropy. One of the special cases important for our research is the impact of a phase retarder on this density matrix. Namely, if a quarter-wave plate (QWP) is introduced into the signal channel (Figure 1), we will expectedly observe a density matrix with the same characteristics and absolute values of the matrix elements, but with nonzero imaginary parts of the anti-diagonal elements:

$$\hat{\rho}^{(QWP)} = \begin{pmatrix} 0 & 0 & 0 & 0 \\ 0 & 0.5 & -0.5\mathrm{i} & 0 \\ 0 & 0.5\mathrm{i} & 0.5 & 0 \\ 0 & 0 & 0 & 0 \end{pmatrix}$$

Here, i is an imaginary unit. This matrix corresponds to the scenario when $\boldsymbol{\varepsilon}_H$-polarized photons pass through the waveplate without change, while $\boldsymbol{\varepsilon}_V$-polarized photons acquire phase shift $\delta = \lambda/4$ due to birefringence. In terms of Jones calculus in our model, this is expressed as

$$\mathbf{X} = \boldsymbol{\varepsilon}_H = \begin{pmatrix} 1 \\ 0 \end{pmatrix}, \quad \mathbf{Y} = \boldsymbol{\varepsilon}_V \exp(\mathrm{i}k\delta) = \begin{pmatrix} 0 \\ \mathrm{i} \end{pmatrix}$$

and $\hat{\rho}^{(QWP)}$ can be immediately obtained from these expressions via Eq. (8) in the main body of the manuscript. As expected, no change is observed in the diagonal elements of the matrix which correspond to the probabilities of the $|HV\rangle$ and $|VH\rangle$ states while the coherencies between them (off-axis elements) are transferred from the real to the imaginary part. The latter indicates the phase delay introduced by the QWP.

Understanding of this effect is important when interpreting the density matrices measured for turbid samples under study. In the experiments (see Materials and Methods in the main text), an auxiliary low-

Read at the publisher: https://doi.org/10.1002/lpor.202501172

focusing lens was found necessary to compensate for the decreased collection of the scattered photons. We have, though, noticed that solely inserting a lens into the optical path alters the detected state. The reconstructed density matrix acquires imaginary anti-diagonal elements, as if birefringence was present in the system (see Figure S1A). Also, the absolute values of the diagonal elements cease to be equal (difference on the level of 1.5%). This phenomenon could be explained by the fact that the lens influences both the polarization state and path lengths of the incident light (*83*), as well as by the induced birefringence which could arise from mechanical stresses caused by mounting the lens.

In order to account for the lens influence on the reconstructed two-photon state in numerical studies, we fitted simulation parameters so that the computed density matrix matches to the one measured in presence of the lens (see Figure S1B). The values of the defined fitting parameters suggest that the presence of the lens in the optical path could result in slightly preferred transmission of the horizontal polarization and exhibit extremely low ($\lambda/26$) level of birefringence (or phase delay due to other effects). The latter is not commonly considered for most of the applications using classical states of light taking into account the negligibility of the effect. However, this becomes critical when dealing with polarization-entangled photon pairs and indicates potentially enhanced sensitivity of the measurement using such and further non-classical states of

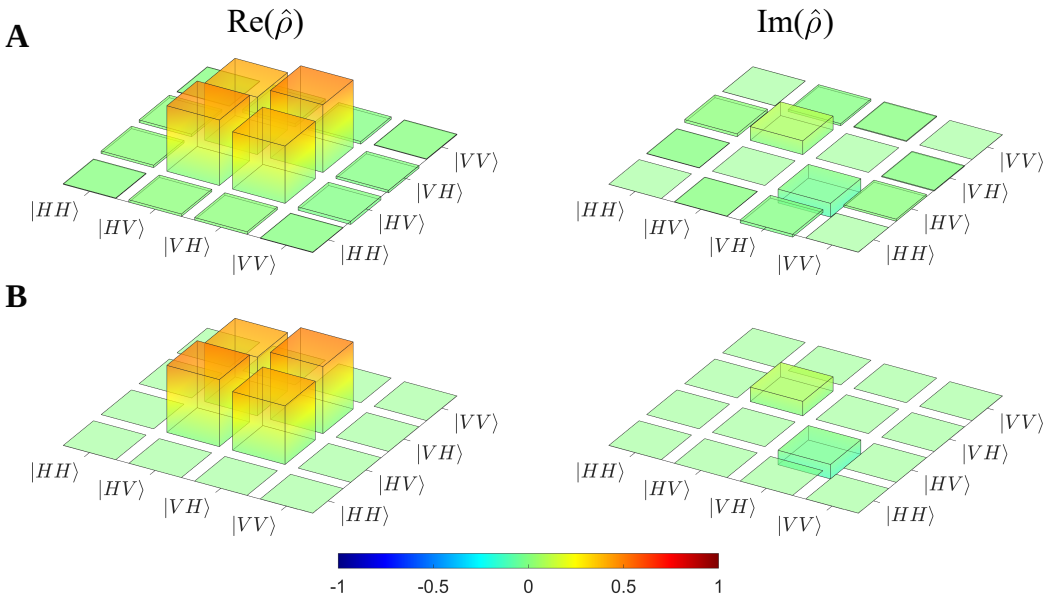

Figure S1: **Impact of auxiliary optics on the probing Bell state**. **A** Measured and **B** simulated density matrix of the state with lens but no turbid sample in the signal channel. Simulated matrix accounts for the phase delay $\delta = -\lambda/26$ which might be explained among others by the possible induced birefringence in the auxiliary lens, as well as for the mix of two linearly independent Bell states (Materials and Methods).

Read at the publisher: https://doi.org/10.1002/lpor.202501172

light (*47*). The discussed issue will be further investigated in our future studies while for the current work we employ the fitted model of the lens.

Details on Monte Carlo implementation

The key steps of the modeling algorithm that we have implemented in the current study is shown in Figure S2. It is already adapted to model the polarization-entangled photon pairs.

First, a large amount of photon packets ($N_{inc} > 10^9$) is launched from the light source. We model the uniform distribution of the photon packets within the cross-section of the beam incident on the sample, and so we launch each (j-th) of these packets with a unit statistical weight W_j. We also supply each photon packet with a polarization vector $\mathbf{P}_0$: for the horizontally polarized state $\mathbf{P}_0 = (1, 0, 0)^T$, and for the vertically polarized state $\mathbf{P}_0 = (0, 1, 0)^T$. Photon packets are launched from the source and propagate without constraints toward the sample interface: in this work, all photon packets are assumed to be normally incident at the interface, i.e., propagation direction vector $\mathbf{s} = (0, 0, 1)^T$ for all packets. Expressions for the polarization vector above are provided with account for the normal incidence. At the interface, all photon packets undergo transmission with respect to the Snell and Fresnel laws (*15*).

Second, after interface interaction, a probabilistic value of the path length is determined for each photon packet with respect to the Beer-Lambert law (*67*):

$$l_i = -\ln\xi/\mu_s$$

Here, we employ a uniformly distributed random number $\xi \in (0, 1]$ and index of the scattering event $i = [1...N]$, and assume that $\mu_a \ll \mu_s$. The obtained value l_i indicates the distance, for which the photon packet will propagate in the turbid medium until the next scattering event:

$$\mathbf{r}_i = \mathbf{r}_{i-1} + \mathbf{s}_i l_i$$

At the same time, statistical weight of the photon packet is attenuated as

$$W_i = W_{i-1} e^{-\mu_a l_i}$$

After the scattering event, the new direction of photon packet propagation $\mathbf{s}_{i+1}$ is randomly chosen with respect to the medium-dependent scattering phase function, which in this case acts as a probability density function. In particular, in this work we use the Henyey-Greenstein (HG) phase function (*15*)

$$p_{HG}(\cos\theta') = \frac{1}{4\pi} \frac{1 - g^2}{\left(1 + g^2 - 2g\cos\theta'\right)^{3/2}}$$

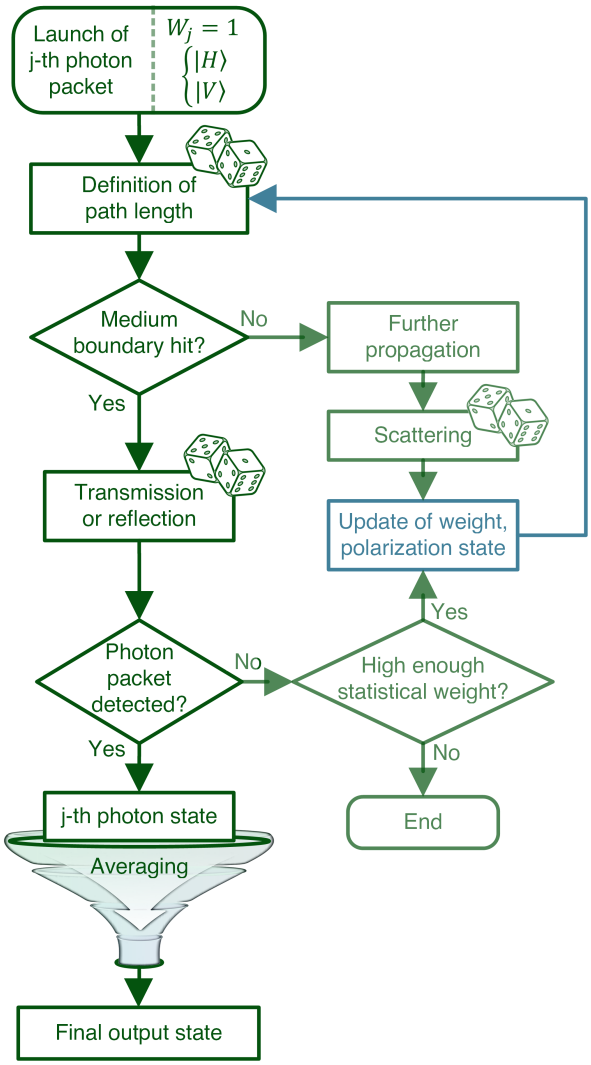

Figure S2: **Conceptual flow chart of the implemented MC model.**

and its inversion:

$$\cos\theta' = \begin{cases} \frac{1}{2g}\left(1 + g^2 - \left[\frac{1-g^2}{1-g+2g\xi}\right]^2\right), & \text{if } g > 0 \\ 2\xi - 1, & \text{if } g = 0 \end{cases}$$

$$\varphi' = 2\pi\xi$$

Here, θ' and φ' are the polar and azimuthal scattering angles in the photon packet reference frame.

We note that if the path of the photon packet crosses the medium boundary (either $z = 0$ or $z = d$, where d is the sample thickness), then instead of the scattering event an interface interaction (i.e., reflection/transmission) event is invoked, which modifies statistical weight with respect to Fresnel law and propagation direction with respect to Snell law. Polarization state of the photon packet can also be updated

Read at the publisher: https://doi.org/10.1002/lpor.202501172

at this step. However, for various cases it appears possible to postpone the evaluation of the polarization state and perform it only for the photon packets which arrived at the detector, leading, e.g., to Eq. (5) in the main body of the paper. We note that this particular equation describes polarization tracing at scattering events and does not account for possible polarization state changes caused by interface reflections.

Finally, photon packets propagate through the turbid medium $0 < z < d$ undergoing a limited amount N of scattering events, and the procedure outlined above repeats N times. Criterion to terminate the propagation of the photon packet originates from the Beer-Lambert law and is either limited by a large amount of scattering events (e.g., $N > 10^3$), or by the negligible statistical weight (e.g., $W_j < 10^{-4}$) obtained due to attenuation and reflection/transmission events. At each reflection/transmission event, part of the photon packet is always assumed to be reflected and continues propagation in the sample, and the other part is assumed to escape from the sample. For this part of the photon packet, detection conditions are checked. These involve either infinite or restricted area of the detector, acceptance angle and other possible limitations (*15*). Those N_{ph} photon packets that arrive at the detector and satisfy the detection conditions finally contribute to the statistics.

Our polarization tracing procedure (defined as Eq. (5) in the main body of the manuscript) requires for both statistical weight and power of the Rayleigh factor $\Gamma_R = 2/\left(1 + \overline{\cos^2\theta}\right)$ of the photon packet to be accounted for along with the detected polarization state $\mathbf{P}_N$ in order to correctly determine its polarization-projected intensity value (*62, 78–80*). Here, $\overline{\cos^2\theta}$ is the square cosine of the scattering angle weighted by the single scattering cross-section (*79*). For instance, in the case when j-photon packet is detected with $\mathbf{X}_j = \mathfrak{m}_j\boldsymbol{\varepsilon}_H + \mathfrak{n}_j\boldsymbol{\varepsilon}_V$ state, corresponding H and V intensity projections can be evaluated as (*15, 79*):

$$I_H\left(\mathbf{X}_j\right) = W_j\mathfrak{m}_j^2\Gamma_R^{N_j}, \quad I_V\left(\mathbf{X}_j\right) = W_j\mathfrak{n}_j^2\Gamma_R^{N_j} \tag{S1}$$

Here, W_j is the detected statistical weight of the j-th photon packet which has propagated through the turbid sample, N_j corresponds to the amount of scattering events along the j-the photon packet trajectory prior to the detection event, and Γ_R is derived from the optical theorem in Born approximation (*62, 78, 80*). We note that in these particular expressions, elements of $\mathbf{X}_j$ are assumed to be real-valued, but in general Jones formalism they can be complex-valued. In this case, square values $\mathfrak{m}^2, \mathfrak{n}^2$ will be replaced by $\mathfrak{m}\cdot\mathfrak{m}^*, \mathfrak{n}\cdot\mathfrak{n}^*$ products. With the above mentioned in mind, expressions which have the form of (S1) can be rewritten in the Dirac bra-ket terms following the Eq. (10) in the main body of the paper. Correspondingly, averaging procedure for these $N_{ph} < N_{inc}$ single photon packets can be written in exactly the same way as Eq. (11) in the main body of the paper by replacing two-photon packet state Φ with the single photon packet state ϕ.

In our MC modeling, we employ the framework of iterative solution to Bethe-Salpeter equation (BSE framework) and thus can track both horizontal $\boldsymbol{\varepsilon}_H$ and vertical $\boldsymbol{\varepsilon}_V$ states along any photon packet trajectory

Read at the publisher: https://doi.org/10.1002/lpor.202501172

simultaneously and independently, while assuming Rayleigh-Gans-Debye approximation (*80*). In fact, this means tracking both polarization states along the same trajectory, which, in general case, might change at one of the later scattering events if the medium exhibits polarization selectivity. The latter is accounted for via probabilistic nature of the photon packet trajectory sampling.

Relation of polarization vector to Jones vector

In this section, we provide details on the relation between Jones vector and polarization vector simulated by the BSE-based MC. For this purpose, in addition to the so-called laboratory Cartesian coordinates (x, y, z) associated with the sample, we introduce local Cartesian coordinates (x', y', z'), where z' axis is always collinear with the photon packet propagation direction $\mathbf{s} = (s_x, s_y, s_z)$. The (x', y') plane in these prime coordinates defines the reference plane of the photon packet.

Jones vector by definition is always expressed in the reference plane $\boldsymbol{\varepsilon} = \left(E_{x'}, E_{y'}\right)^T$ and corresponds to the prime electric vector $\mathbf{E}' = (E_{x'}, E_{y'}, 0)^T$. When expressed in terms of the laboratory Cartesian coordinates, the same electric vector can generally obtain the third component $\mathbf{E} = (E_x, E_y, E_z)^T$. This can be demonstrated by utilizing the proper transition matrix:

$$\mathbf{P} \propto \mathbf{E} = \begin{pmatrix} E_x \\ E_y \\ E_z \end{pmatrix} = \begin{pmatrix} \cos\theta\cos\varphi & -\sin\varphi & \sin\theta\cos\varphi \\ \cos\theta\sin\varphi & \cos\varphi & \sin\theta\sin\varphi \\ -\sin\theta & 0 & \cos\theta \end{pmatrix} \begin{pmatrix} E_{x'} \\ E_{y'} \\ 0 \end{pmatrix}$$

Here, $\theta = \arccos\left(s_z/|\mathbf{s}|\right)$ is a polar angle of the photon packet direction vector $\mathbf{s}$ and φ is an azimuthal angle of this vector expressed in terms of the spherical coordinate system which corresponds to the introduced laboratory Cartesian coordinates. To track evolution of the polarization state of the photons experiencing scattering, we have introduced vector $\mathbf{P}$. We do so in the laboratory Cartesian coordinates, and with the proportionality sign we emphasize that $\mathbf{P}$ vector corresponds to the $\mathbf{E}$ direction (*15*). It is necessary to account for the statistical weight of the photon packet and for the power of the Rayleigh factor Γ_R in order to evaluate corresponding intensity projections.

Thereby, in this work we rely on the fact that it is always possible to interchange between (x, y, z) and (x', y', z') coordinate frames by using proper transition matrix. We point out that the connection between the introduced $\mathbf{E}'$ and its counterpart $\mathbf{E}$ is always known. This connection also enables to link Jones vector $\boldsymbol{\varepsilon}$ and electric field $\mathbf{E}$ vectors, and, correspondingly, $\boldsymbol{\varepsilon}$ and $\mathbf{P}$ vectors for each photon packet. Given that $\mathbf{P}$ is always orthogonal to the propagation direction of the photon packet, Jones vector components can always be reconstructed by using the reverse transition matrix (*59*).

Read at the publisher: https://doi.org/10.1002/lpor.202501172